

**PREPRINT SUBMITTED, PEER-REVIEWED, CHANGES NOT IMPLEMENTED**

This manuscript is a **preprint** uploaded to **EarthArXiv**. This preprint has been **submitted** for publication to **TECTONICS** on the **21/05/19**. This preprint version has implemented the comment of an earlier submission and peer-review in GEOLOGY. Newer versions may be slightly different with moderate variations in content. Authors encourage downloading the latest manuscript version from EarthArXiv before usage. Authors welcome comments, feedback and discussions anytime.

Please, feel free to get in contact: [geo.david.fernandez@gmail.com](mailto:geo.david.fernandez@gmail.com)

# Geometry of flexural uplift by continental rifting in Corinth, Greece

David Fernández-Blanco, Gino de Gelder, Robin Lacassin & Rolando Armijo

Université de Paris, Institut de physique du globe de Paris, CNRS, F-75005 Paris, France

## Abstract

Understanding early rifting of continental lithosphere requires an accurate description of up-bended rift margins and footwalls that correlates, both in space and time, with the elastic flexural uplift that produces them. Here, we characterize the geometry of elastic flexural uplift by continental rifting at its spatiotemporal scale in nature (10s km;  $10^4$ - $10^6$  yr) using geomorphic evidence throughout the uplifting margin of the Corinth Rift, Greece. Our geomorphic analyses of space-borne topography novelly outline the coherent elastic flexure of continental lithosphere, along and across the rift margin and throughout faulting ( $\sim 10^6$  yr), defined by a distribution of footwall uplift south of the active bounding fault. Topography and river drainages outline an exponential increase of the elastic flexure towards the bounding fault, across-footwall for  $>50$  km, varying in along-footwall amplitude in a parabola that decays from the rift center and has a wavelength ( $>60$  km) that correlates with the length of the rift. The continental lithosphere up bend appears maximum in the centre of the rift, where drainage reversal large catchments suggests rapid slip rates at the bounding fault, and decays gently to the west and sharply to the east. This is consistent with the growth of a new rift-scale, high-angle normal fault. The coherency of elastic flexure in space and time implies highly-localized strain in such rift-bounding fault and suggest that it transects continental lithosphere with long-term strength. Corinth landscape unparalleled record of flexural uplift and highly-localized strain suggest these processes are intrinsic to early continental rifting.

*Keywords: elastic flexure; normal fault; rift margin; footwall rivers; footwall topography; Corinth Rift*

## Introduction

Numerical models show that crustal-scale elastic flexure and localized strain occur in the flanks of high-angle normal faults transecting continental lithosphere (e.g., Buck, 1993; King & Ellis, 1990). Elastic flexure leads to fault flank uplift and subsidence that span for tens of kilometers along strike and decay exponentially across strike within few tens of kilometers (Fig. 1A) (King & Ellis, 1990; Weissel & Karner, 1989). Similar flexural strain, albeit of much smaller amplitude, occurs in high-angle faults during  $M_w \geq 6$  earthquakes, suggesting that cumulative seismic events may result in km-scale long-term flexural relief (King et al., 1988). By contrast, low-angle faults develop little to no elastic flexure (Fig. 1B) (e.g., Forsyth, 1992). Footwall up-warping in continents is particularly interesting, for the up-flexed topography can be used to discriminate between low- and high-angle extensional faulting (Bell et al., 2017), and the wavelength and curvature of flexural uplift to infer relative strength layering of the underlying lithosphere (e.g., Armijo et al., 1996; De Gelder et al., 2019). Nevertheless, these and other inferences on lithosphere strain, mechanics and rheology are limited to the spatiotemporal scale and overall detail at which flexure is characterized in nature.

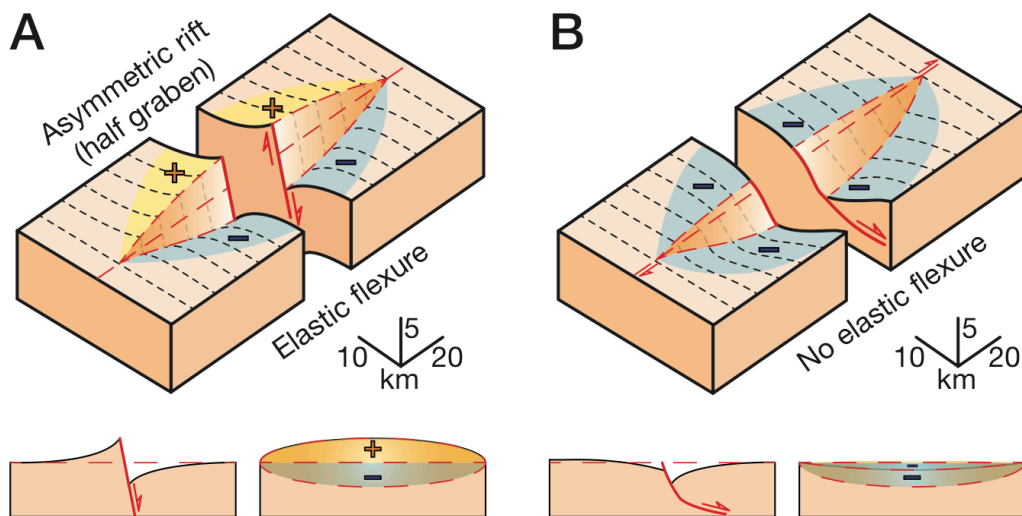


**Fig. 1. Block diagrams of vertical motions led by high- and low- angle normal faults.** (A) Block diagram with flexural footwall uplift and flexural hanging-wall subsidence expected in relation to a high-angle planar normal fault. (B) Block diagram with footwall and hanging-wall subsidence expected in relation to a low-angle detachment normal fault. Across (left) and along (right) fault strike views are shown below each case.

Lithospheric elastic flexure in extensionally uplifted rift margins and footwalls produces short-wavelength tilts that sporadically steer drainage reversals in large Cenozoic continental rifts, like the East African and Baikal rifts, and in individual grabens within wider areas of diffuse extension, like the Basin and Range and Tibet (e.g., Armijo et al., 1986; Doornkamp & Temple, 1966; Petit & Ebinger, 2000; Stewart, 1978). Research in these areas uses flexure geometries derived from relatively imprecise observations of topography to deduce rift mechanics and/or geodynamics (e.g., Brown & Phillips, 1999; Masek et al., 1994; Owens, 1983; ter Voorde et al., 1998; Zandt & Owens, 1980). Finer characterisations of flexure geometry leading to better-constrained results are either precluded by scant unambiguous geomorphological evidence in relatively old ( $>10^6$  yr) regions (e.g., Stein et al., 1988) or restricted to individual transects (Armijo et al., 1996; De Gelder et al., 2019) and/or short temporal scales ( $<10^3$  yr) (e.g., Thompson & Parsons, 2016).

This paper aims at defining the flexural uplift geometry due to continental rifting at its spatiotemporal scale in nature (tens of km;  $10^4$ - $10^6$  yr). We combine footwall topography and river catchments to explore the existence, geometry, coherency and extent of flexural uplift, resolving its across- and along-strike components with morphotectonic analyses grounded in fault mechanics. For this, we use space-borne digital elevation data covering the southern, uplifting margin of the rapidly-extending Corinth Rift, in Central Greece (Fig. 2). Topography, rivers and morphometric proxies throughout the rift margin novelly portray elastic flexural uplift, highly-localized strain and large lithospheric strength coherently sustained in space ( $>50$  km across and along rift margin) and time ( $\sim 10^6$  yr). Given that the Corinth Rift outstands worldwide by its record of early continental rifting, we infer that elastic flexure and high strain localization are intrinsic processes of early continental rifting. This inference implies that elastic flexure and high strain localization may have occurred in continental rifts and extensional footwalls of any age or extension rate, even without equivocal evidence of these processes.

## 2 Corinth Rift: Early continental rifting natural laboratory

After a period of distributed extension and faulting, the amagmatic continental rift of Corinth is at a very early rifting stage in relation to its current rift-bounding fault system (Bell et al., 2017) (Main fault system, Fig. 2). Rollback of the African slab leading to the southward retreat of the Hellenic trench since ~30-45 Ma (e.g., Brun & Sokoutis, 2010; Jolivet et al., 2013; Jolivet & Brun, 2010; Le Pichon & Angelier, 1981) is probably the cause of fault basinward migration and block tilting that started distributed extension in the area 4-5 Ma (e.g., Doutsos & Piper, 1990; Gawthorpe et al., 1994; Goldsworthy & Jackson, 2001). At 1 Ma or younger times, the onset of activity of the north-dipping high-angle fault system that currently bounds the rift southern margin (Main fault system; Fig. 2) (e.g., Armijo et al., 1996; Nixon et al., 2016) led to a rapid increase in tectonic rates and ensued a prominent elastic flexure that has been characterized in detail in the rift east sector (Fig. 3) (Armijo et al., 1996; De Gelder et al., 2019). The Main fault system accommodates faster geodetic strain rates ( $\sim 1-1.5 \text{ cm}\times\text{yr}^{-1}$ ) (Avallone et al., 2004) than any subaerially-exposed normal fault on Earth (Charalampakis et al., 2014; Tetreault & Buitter, 2018) and has remarkable seismic activity (e.g., Bernard et al., 2006). Rapid Quaternary coastal uplift suggests fast localisation of extension in relation with this fault system (Roberts et al., 2009), which probably has larger uplift at the rift centre (e.g., Dufaure, 1975; Pirazzoli et al., 2004). Footwall uplift rates of  $\sim 1 \text{ mm}\times\text{yr}^{-1}$  for the last  $\sim 330 \text{ ky}$  notably exceed regional uplift rates of  $\sim 0-0.3 \text{ mm}\times\text{yr}^{-1}$  (e.g., Armijo et al., 1996; McNeill & Collier, 2004; Turner et al., 2010) and set, atop inherited relief (e.g., Ghisetti & Vezzani, 2005; Hemelsdaël et al., 2017; Ori, 1989), the modern rift asymmetry. By the above, the southern, uplifting margin of the Corinth Rift is an exceptional site to constrain the geometry of flexure (Figs. 2 & 3).

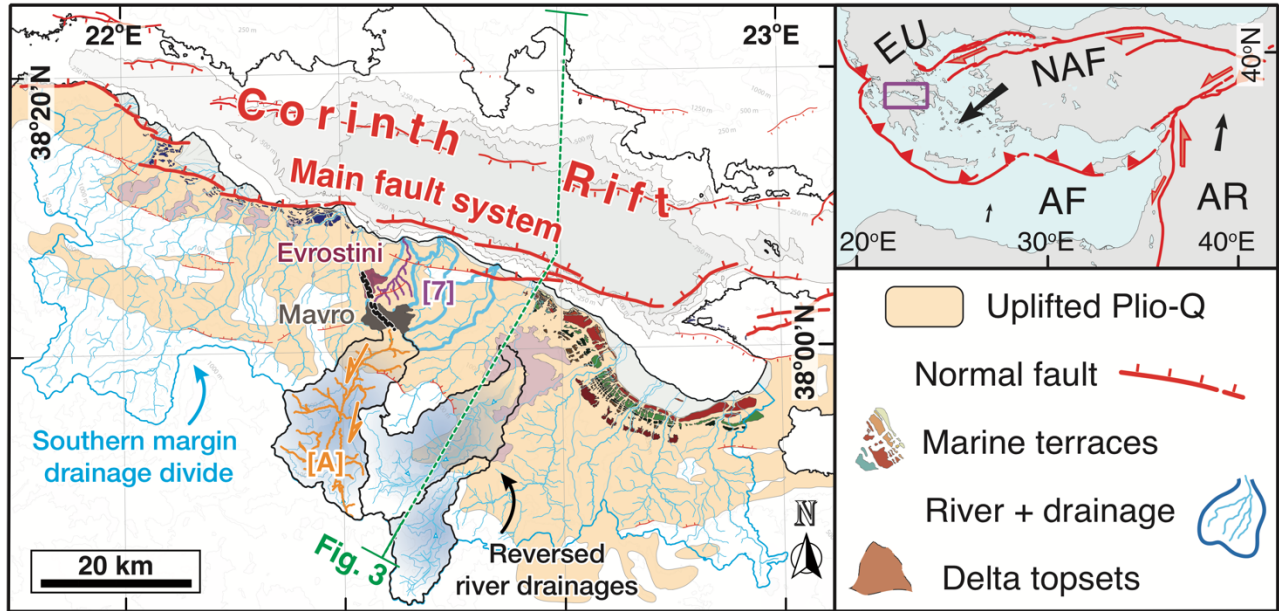


**Fig. 2. Corinth Rift active tectonics map.** Corinth Rift map highlighting geomorphological and geological features associated with the Main fault system, in red. Drainage basins are shown in blue, the uplifted Plio-Q basin infill in yellow, uplifted marine terraces and perched Gilbert-type deltas are in several colours and in light purple, respectively. Watersheds of steep and short beheaded rivers are in thicker blue stroke, with the Dervenios River [7] in purple as representative for this group. Watersheds of endorheic drainages are in black stroke, with the Olvios River [A] in orange, as their reversed-flow representative. South tilted plains are shaded in blue. Map also shows the windgaps in Mavro and Evrostini Gilbert delta, and the location of the on- and offshore cross-section in Fig. 3.

In the east rift, elastic flexure on the main fault flanks sets the modern asymmetry (Fig. 3). An extensive flight of exceptionally preserved marine terraces in the eastern footwall (Armijo et al., 1996), and prominent syntectonic sedimentary wedges of correlatable seismic horizons in its hanging-wall (Taylor et al., 2011) record an exponential increase in elastic flexure amplitude toward the rift bounding fault (Fig. 3) (De Gelder et al., 2019). Markers show the growth of ~4.8 km of structural relief since the onset of bounding fault activity, 800-600 ka, which localized strain over a ~300 kyr interval (Nixon et al., 2016). Flexural uplift on  $10^4$ - $10^6$  yr timescales is recorded by the Late Pleistocene marine terraces (Figs. 2 & 3) (Armijo et al., 1996; De Gelder et al., 2019). If a similar signal of flexural uplift exists also westwards, it should be recorded along the rift margin in its geomorphological evidence.

In the central rift, south-tilted Middle Pleistocene conglomerates of deltaic systems are carved by windgaps that bound formerly connected drainages (Dufaure, 1977). Steep and short beheaded catchments drain toward the gulf, northward of large, reversed drainages that now are at heights of 700-800 m and infill flat sedimentary plains with a gentle tilt south (Figs. 2 & 3) (Seger & Alexander, 1993). The uppermost abandoned valley is carved in the oldest delta (Mavro) and aligns with the windgap of a younger delta (Evrostini) located northwestward at lower elevations (Fig. 2) (e.g., Rohais et al., 2007). This is, the same river bypassed the former delta to feed the latter. Such configuration of windgap-bounded drainages imply drainage reversals at large scale (e.g., Dufaure, 1977) and may result from footwall flexural uplift (Armijo et al., 1996). Being this the case, footwall flexural uplift would postdate Mavro Delta deposition and predate Evrostini Delta deposition, which chrono- and lithostratigraphical correlations set at  $\sim 0.7$  Ma (Ford et al., 2016).

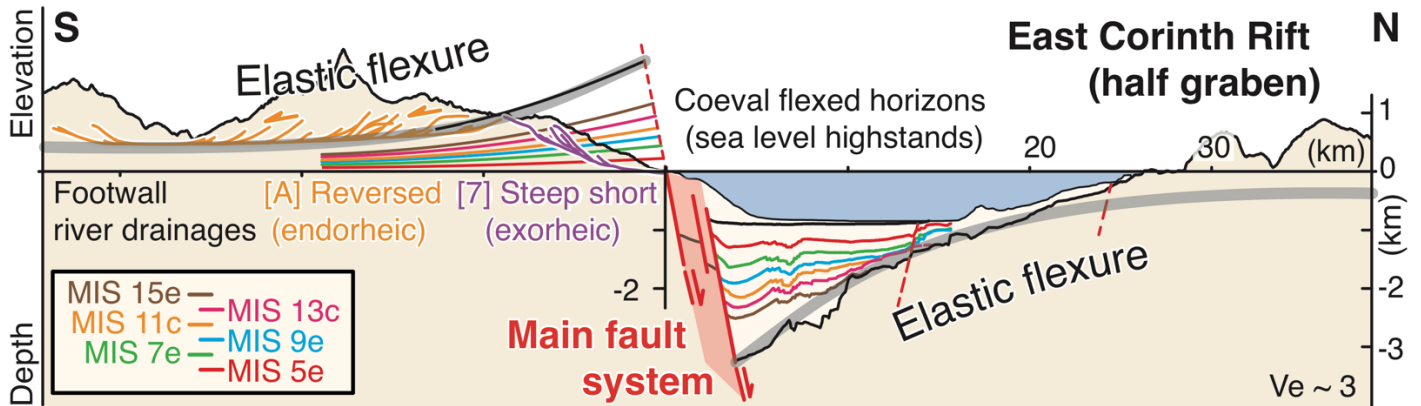


**Fig. 3. Onshore-offshore cross-section across the eastern Corinth Rift.** Onshore-offshore cross-section showing elastic flexure as detailed by coeval markers of sea level and river profiles projected towards the section located in Fig. 2.

Paleohorizons in different colours represent major sea level highstands (see inset in the lower left) that have been derived from best-fit quadratic curves of up-flexed terraces in the onshore (De Gelder et al., 2019) and their tentatively correlatable seismic horizons in the offshore (Nixon et al., 2016) on the seismic line L35 of Taylor et al., (2011), depth-converted as in de Gelder et al., 2019. Modified after Fig. 3 of de Gelder et al. (2019).

In the west rift, westwards of the reversed drainages, river morphology of the largest catchments is similar albeit less marked; steep gorges and narrow valleys in a broad up-warped zone (e.g. knickzone) separate a low-gradient low-relief upstream landscape from a steeper, higher relief landscape downstream (e.g., Seger & Alexander, 1993). As in the rift centre, west rift sequences of offlapping stranded deltas become younger coastward (Ford et al., 2012, 2016; Seger & Alexander, 1993). This, and former hanging-wall sediments uplifted by sequentially younger footwalls, suggest basinward migration of border fault systems (e.g., Gawthorpe et al., 2017). No proposal of elastic flexure is made to explain the evolution of the west rift sector, and no evidence of footwall flexural uplift has been documented.

### **3 Working framework & hypotheses**

Given that the long-term slip and derived uplift patterns on bounding fault(s) control the long-term morphological evolution of rift margins and footwalls (e.g., Cowie & Scholz, 1992), the landscape in these uplifted settings can be used to understand their controlling fault(s) (e.g., Cowie et al., 2006). High-angle normal faults have a predictable geometry of slip and slip rates along strike and uplift and uplift rates across strike. Along-strike, slip and slip rates parabolically decay from a maximum near the fault centre to zero at fault tips (e.g., Bürgmann et al., 1994; Cowie & Scholz, 1992; Dawers et al., 1993; Manighetti et al., 2001; Roberts & Michetti, 2004). Such distribution of slip and slip rates control the geometry and geomorphic evolution of along-footwall topography and river catchments (e.g., Densmore et al., 2004, 2005; Kent et al., 2016; Roda-Boluda & Whittaker, 2017). Across-strike, uplift and uplift rates exponentially decay from maxima near the fault to zero few tens of kilometres away (e.g., King et al., 1988; King & Ellis, 1990; Thompson & Parsons, 2016). Such distribution of uplift and uplift rates control the geometry and geomorphic evolution of topography across the footwall (Armijo et al., 1996; De Gelder et al., 2019; Stein et al., 1988), but their effect on river catchments remains unexplored. The above implies that we can anticipate the morphological



evolution for footwalls uplifting in relation to range-front high-angle normal faults (Armijo et al., 1991; Armijo et al., 1986; Wallace, 1978).

The geometry of topography flexed up towards the bounding fault is often used to define the exponential increase in flexural uplift signal across extensional footwalls (e.g., Brown & Phillips, 1999; Masek et al., 1994; Owens, 1983; Stein et al., 1988; ter Voorde et al., 1998; Zandt & Owens, 1980) but the along-footwall signal of flexural uplift is still unlinked with the topography it shapes. Intuitively, the along-footwall shape of flexed topography should link with the fault displacement profile. Similarly, the along-footwall extent of flexed topography should correlate with fault length and its coherency should relate with the degree of strain localisation at the fault.

River catchments are commonly used to resolve uplift signals and slip rates in extensional rift margins and footwalls (Boulton & Whittaker, 2009; Gallen & Wegmann, 2017; Kirby & Whipple, 2012; Miller et al., 2012; Whittaker, 2012; Whittaker et al., 2008; Wobus et al., 2006). However, the influence of elastic flexure in footwall rivers remains to be explored. This gap may result from the fact that morphometric analyses using drainage basin-scale metrics (Demoulin et al., 2015) are not suited for cases of flexure, for they average the spatially varying strike-perpendicular component of uplift across catchment. The exception is Goren et al. (2014), where an expected flexural response to normal faulting is used in linear inversions that parametrize uplift spatial variability in the Inyo Range, California. There, footwall rivers are short (<10 km in length) and their profile morphology is not used to infer the flexural uplift signal, that is treated as an input to their models. Therefore, how elastic flexure in these settings influences river morphology remains to be explored, and inversely, so does how river morphology may inform about the scale, geometry and uplift patterns of the fault accommodating flexure.

Footwall rivers that drain orthogonally towards the range-front fault should experience the maximum gradient in flexural uplift. We expect that these rivers have transitional longitudinal profiles that departure from their homogeneous-uplift theoretical graded profiles. Instead, such

transitional longitudinal profiles should have steep lower reaches adjusted to near-fault uplift, followed by anomalously low-gradient reaches immediately upstream, as the across-footwall flexural uplift decays exponentially away from the fault. If this were the case, landward drainage tilts should be larger with larger uplift, and thus larger slip at the fault. This would drive the sediment starvation by rift margin tilting (Pechlivanidou et al., 2019), as acute drainage back-tilts will lower the river erosion capabilities. Therefore, prominent flexural uplift may lead to an end-member case that forces drainage disruption in two, an upstream perched low-gradient river with reversed flow, and a beheaded steep river downstream. Along-footwall, the heights of near-fault transitions from steep to gentler reaches should also positively correlate with fault uplift and slip. The along-footwall continuity of the flexure signal should relate with the displacement profile of the associated fault and correlate with its length. Therefore, longitudinal profiles of successive rivers laying orthogonal to the fault can provide along-footwall coverage and portray the lateral extent of flexure, and thus potentially discriminate the effects of one or more faults.

#### **4 Methods and assumptions**

We use 20m-resolution digital elevation data to examine footwall topography, relief and river longitudinal profiles throughout the rift margin, as well as geomorphic proxies of uplift and uplift rate that we relate with displacement, slip and slip rate on the bounding fault system. We analysed footwall topography and river profiles in the rift margin sector where the bounding fault has a continuous strike length of ~60 km (Fig. 2). This “main sector” includes 11 of the 16 largest rivers catchments draining north, almost orthogonally toward the master fault, and the 3 catchments with reversed drainage, now flowing inland toward their former headwaters (Fig. 2).

## 4.1 Digital Elevation Models (DEMs)

We used the 30-m horizontal resolution ALOS AW3D30 DSM (ALOS) and patched voids and gaps with ASTER GDEM V2 (ASTER) for an area inclusive of the whole Peloponnese and both margins of the Gulf of Corinth. We upsampled the merged DEM for latitudes north of Nafplion with a 20-m horizontal (post-spacing) resolution SPOT5 DEM of an area that covers the southern shoulder of the Corinth Rift, the Perachora Peninsula and the Kaparelli area. We then clipped the composite DEM using drainage areas of Peloponnesian rivers discharging into the gulf and the three largest reversed rivers that are now endorheic basins, i.e. Feneos, Stymfalia and Skotini. These areas with internal drainage were manually delineated to avoid the inaccuracies of automatic methods.

## 4.2 Stacked swaths

Stacked swaths (or wide swath) are large numbers of parallel swaths jointly projected as hairlines orthogonal to their trends (stacked). Stacked swaths can be used to highlight the coherence of topography and thus the continuity of morphological features in three-dimensions over large scales (Armijo et al., 2015). We use stacked swaths to portray the rift margin footwall topography, including its three largest reversed river catchments, for ~60 km along rift margin strike (Fig. 2). We use 300 parallel swaths profiles derived from our DEM and stack them orthogonally to the average strike of the active master fault system (taken as N105°E) and plotted them looking WNW. The width of each individual swath is defined dynamically by dividing DEM width along the projection direction by the number of swath profiles.

## 4.3 Footwall relief

The mountain front relief of an uplifting extensional footwall results from long-term uplift, and thus slip of its bounding fault. Range front relief shows the cumulative fault displacement and can be used to infer the dimensions of the active fault and its history of growth and linkage (e.g., Dawers & Anders,

1995; Gupta & Scholz, 2000). We use the footwall relief, a proxy to range front relief. We define and calculate footwall relief along the rift margin in a similar fashion to Whittaker and Walker (2015). We consider footwall relief as the absolute difference in elevation, measured vertically, from the trace of the fault to the first prominent topographic break in slope in the footwall topography, which represents the crest of frontal relief, set by the main triangular facets in the footwall. The first topographic break of slope is observed in the footwall topography at distances of <20km, often ~15km, measured inland perpendicularly from the fault trace strike. Consequently, we visually defined a polygon in the DEM that covers the inflection, extending inland for ~21km perpendicular to the fault strike at each fault sector. This polygon removes topography farther away from the fault and facilitates recognition of the first break of slope in the footwall topography.

We use this polygon along the “main” sector to calculate ~20m-wide swaths each 20m, that are orthogonal to the fault trace strike. We calculate the position of the first break of slope, and project it along fault strike, and graphically attach an estimated uncertainty derived from two factors: confidence in the accurate mapping of the fault trace, and the discrepancy between fault strike and chosen direction of projection. The master fault can be confidently mapped in the west of the main sector, where uncertainties associated with the position of the fault trace are minimal. Eastwards, the position of the master fault is more imprecise as the fault lays underwater and its trace can be mapped with less accuracy. We estimate a maximum vertical uncertainty of ~250 m for the eastern main sector due to this effect in combination with the unconstrained growth behavior of the footwall relief underwater. We further attribute a maximum estimated uncertainty of  $\pm 50$  m to the discrepancy between our chosen projection plane and the fault strike towards the eastern areas of the main sector. We consider the equivalent uncertainty negligible in the western main sector.

#### 4.4 Longitudinal river profiles

First order clues on the evolution of normal fault systems can be deduced from local convexities (knickpoint zones) in the longitudinal profiles of footwall rivers. For example, a change in rock uplift rate will lead to the upstream migration of a knickpoint as a kinematic-wave, and the river channel will steepen in the wake of the passing knickpoint (Rosenbloom & Anderson, 1994). The knickpoint acts as a mobile boundary between a former portion of the stream unaware of a change in uplift rate and an adjusted or adjusting downstream reach (e.g., Snyder et al., 2000; Whipple & Tucker, 1999). We used Topotoolbox 2.0 (Schwanghart & Scherler, 2014) to extract the river profiles and  $\chi$  Profiler package (Gallen & Wegmann, 2017) for river profile analysis. Fluvial channels were defined as areas draining  $\geq 10^6$  m<sup>2</sup> and smoothed with a 500 m moving window average.

To portray the river network morphology and the longitudinal profiles of the three reversed, endorheic river catchments, with flows that do not reach the regional base level, we performed specific corrections. We set an artificial outlet by creating a sink at the lowest point of the longest stream, and clipped the DEM in the drainage areas north and south of it. We performed stream flow direction and other suitable procedures as for the rest of the rivers. We oriented the outcome of the longitudinal river profiles according to their general flow direction, i.e. one flowing northwards and one southwards. The resulting longitudinal profile was oriented to match the flow direction in the longitudinal profiles of exorheic rivers.

#### 4.5 Height of the main inflections

River profile inflections have vertical rates of propagation that are a function of the change in the rate of footwall uplift (Attal et al., 2008; Crosby & Whipple, 2006; Whittaker et al., 2008; Wobus et al., 2006). Provided uniform climate and substrate properties, knickpoints resulting from a temporal change in uplift rate will propagate vertically at the same rate (Niemann et al., 2001). Along normal faults, which typically show variable rates of uplift along strike, the relative height of knickpoints is

a function of this differential along-strike uplift (e.g., tectonic knickpoints at higher positions may be linked to faster fault throw rates) (Whittaker et al., 2008; Whittaker & Walker, 2015). We derive the height of the principal inflection of river catchments flowing towards the hanging-wall, and including both, the height of main knickpoints of trunks longitudinal profiles for rivers flowing towards the gulf, and the height of the windgaps, approximated by the highest point of the behaved rivers. Knickpoint height depends on the relative throw rate increase along the driving fault strike (e.g., Whittaker & Walker, 2015), and can thus be used as a proxy for the magnitude of along-footwall uplift that ultimately relates to the distribution of slip along the fault.

#### 4.6 Normalized steepness index (ksn) below the principal inflections

Researchers have demonstrated that there is a functional relationship between rock uplift rate or erosion rate and river channel steepness normalized upstream by contributing drainage area, which suggests that river channel steepness can be used as a proxy for relative rate of uplift or erosion (Snyder et al., 2000; Ouimet et al., 2009; DiBiase et al., 2010; Gallen and Wegmann, 2017). These empirical studies are supported by quasi-physical models of river incision that imply that bedrock river incision is related to upstream drainage area, a proxy for discharge, and local channel slope (Howard, 1994; Whipple and Tucker, 1999; Tucker and Whipple, 2002). The most general of these models is the detachment-limited stream power incision model, which, when combined with mass-conservation, describes the change in river bed elevation over time as follows,

$$\frac{dz}{dt} = U - E = U - KA^m S^n \quad (1)$$

where  $dz/dt$  is the change in elevation of the channel bed with time,  $U$  is rock uplift rate relative to a fixed base level,  $E$  is river erosion,  $A$  is the upstream drainage area,  $S$  is local channel slope,  $K$  is a dimensional coefficient that incorporates variables dependent on incision process,

substrate, climate and hydrology of erosion (e.g., Whipple, 2004), and  $m$  and  $n$  are positive constants that depend on basin hydrology, channel geometry, and erosion processes (Howard, 1994; Whipple, 2004; Whipple and Tucker, 1999). Assuming steady-state conditions where rock uplift rate and erosion rate are equal, local channel slope can be cast as a function as,

$$S = (U/K)^{1/n} A^{-(m/n)} \quad (2)$$

Equation 2 has the same form as Flint's (1974) law, which describes the equilibrium geometry of a longitudinal river profile as a power law function of upstream contributing drainage area through the channel parameters of the steepness index and concavity index. The steepness index is proportional to the ratio of rock uplift to substrate erodibility and the concavity index is equal to the ratio of  $m$  to  $n$  (Kirby and Whipple, 2001; Snyder et al., 2000).

The river channel concavity, defined as  $\theta$  or  $m/n$ , is theoretically independent of rock uplift rate or erosion rate but will strongly impact the steepness index of the river. In an effort to remove the influence of channel concavity on the steepness index many researchers use a fixed reference concavity index, defined as  $\theta$  ( $m/n$ ), to derive a normalized steepness index,  $k_{sn}$ . From theory, the concavity index ( $\theta$ ) should vary between  $\sim 0.3$  to  $0.7$ , and many empirical studies find a value of  $\sim 0.45$  for most river profiles near equilibrium or graded conditions (Kirby and Whipple, 2012; Snyder et al., 2000; Wobus et al., 2006). Thus, most researchers use a reference concavity of  $0.45$ , as is used in this study, to calculate the normalized steepness index and assess relative patterns of rock uplift in space and time.

Traditionally,  $k_{sn}$  is calculated by a linear regression of  $\log S$  and  $\log A$  (Kirby and Whipple, 2012); however, Perron and Royden (2013) recognized that this approach introduces unwanted noise in the data and they propose the integral or  $\chi$  method of river profile analysis instead. The  $\chi$ -analysis relies on a transformation of the horizontal coordinate for a river profile, from distance to  $\chi$ ,

where  $\chi$  is an integral quantity with units of length. Separating variables in Eq (2), assuming  $U$  and  $K$  are spatially invariant, and integrating yields:

$$z(x) = z(x_b) + \left(\frac{U}{K}\right)^{\frac{1}{n}} \int_{x_b}^x \frac{dx}{A(x)^{m/n}} \quad (3)$$

Where  $z$  is elevation and  $x_b$  is base level. The trailing term on the right-hand side of the equation is unitless. Therefore, a reference drainage area  $A_o$  is introduced such that:

$$z(x) = z(x_b) + \left(\frac{U}{KA_o^m}\right)^{\frac{1}{n}} \chi \quad (4)$$

Where:

$$\chi = \int_{x_b}^x \left(\frac{A_o}{A(x)}\right)^{m/n} dx \quad (5)$$

Equation 5 is convenient because it has the form of a line where  $z$  is the dependent variable,  $\chi$  is the independent variable,  $z(x_b)$  is the y-intercept and  $\left(\frac{U}{KA_o^m}\right)^{\frac{1}{n}}$  is the slope. Plots of  $\chi$  and  $z$  are referred to as  $\chi$ -plots. It is important to recognize that when  $A_o$  is assumed to be 1, the slope in a  $\chi$ -plot is the same as  $k_{sn}$ , thus it is best practice to always use an  $A_o$  equal to 1 to standardize  $\chi$ -plots (e.g., Gallen and Wegmann, 2017).

Being a metric sensitive to the rock uplift rate (Snyder et al., 2000), we calculate the values of the  $k_{sn}$  of river streams below the main inflection as proxies for the magnitude of along-footwall uplift rate and thus the distribution of slip rate along-strike in the active fault system, providing that



erodibility and climatic variations are minor with regards to variations in rock uplift (Kirby & Whipple, 2001). we use  $k_{sn}$  values.

## 5 Results: Landscape record of flexural uplift

We characterize the long-term activity of the bounding fault along the main rift sector analysing the geometry of morphotectonic features and metrics in relation to the active fault.

### 5.1 Across-footwall topography

We analyze the geometry of the across-footwall topography (Fig. 4) by means of swath topographic profiles stacked orthogonally to the active fault. Across-footwall stacked-swath profiles show that topography is self-consistent throughout the main sector along its strike ( $\sim 60$  km) (Fig. 4A) and agrees with the flexural uplift signal derived from paleoshoreline angles of marine terraces located immediately eastward (cf. Figs. 3 & 4A). The topography shows a stark transition across the footwall, from a steep coastal topography up to  $\sim 1.5$  km in elevation at  $\sim 15$  km from the bounding fault into a flat topography sloping southward  $< 300$  m over horizontal distances of  $> 35$  km (Fig. 4A). The across-footwall topography in the rift center (Fig. 4B) shows a sharper transition between the steep coastal slopes and gentle inland slopes than footwall topography farther west (Fig. 4C). Similarly, the along-footwall topographic change seems to locate closer to the fault and at higher elevations in the eastern than in the western region of the footwall main sector (cf. Figs. 4B & 4C). The along-footwall consistency of topography is remarkable, and larger in the eastern main sector of the rift margin, where topography tilts southward markedly, than in the western main sector (cf. Figs. 4B & 4C). The above suggests that the topography of the main rift sector responds to flexure as a whole and in a similar manner than the Late Pleistocene marine terraces, and thus that the flexural uplift signal controlling the latter is sustained on the long term ( $\sim 10^6$  yr) and dominates at least the main sector of the rift margin.

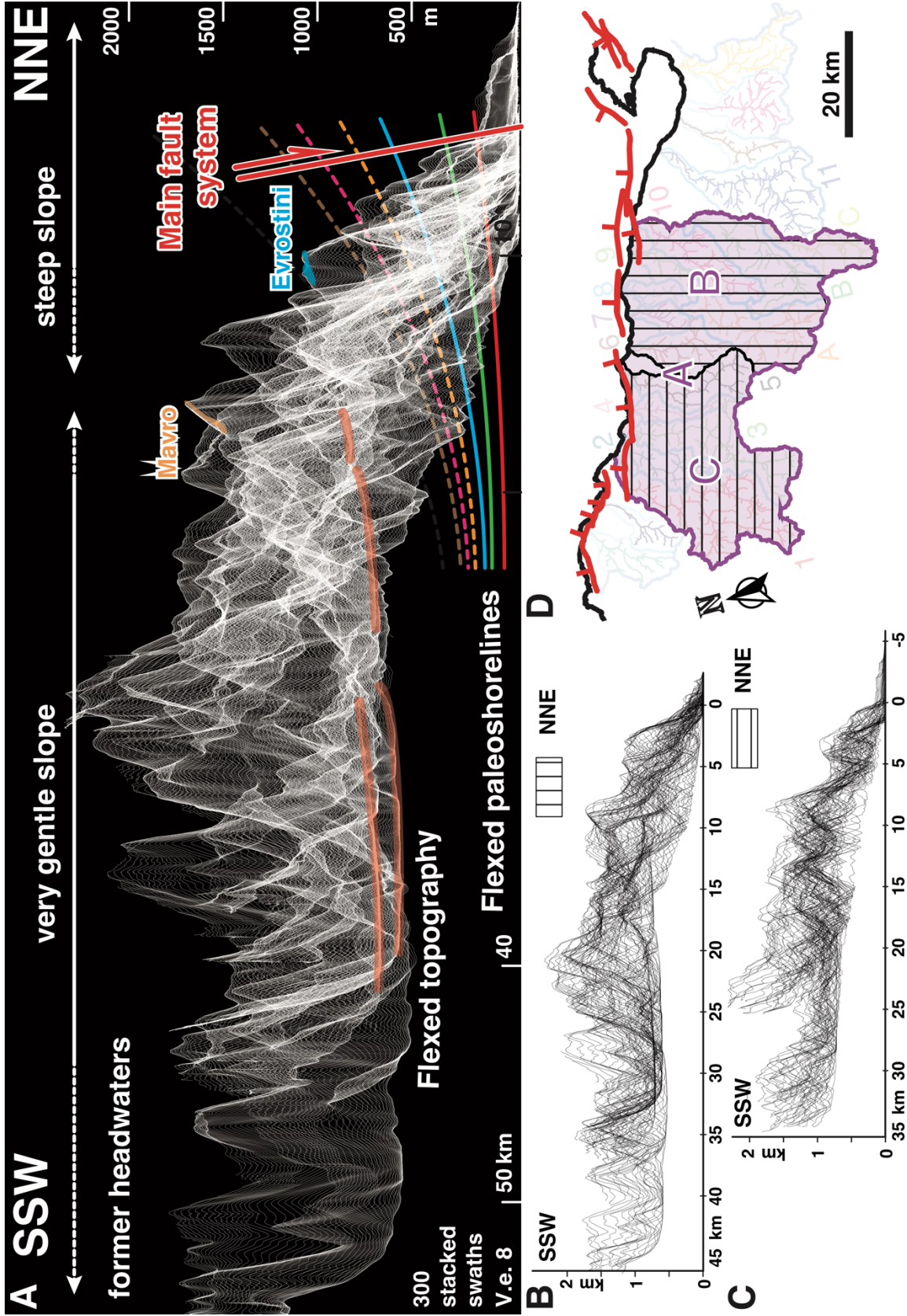


**Fig. 4. Across-footwall topography.** (A) View of topography perpendicular to the bounding fault strike along the entire main sector (defined in section 4), looking WNW. The DEM area covered is shown in purple (as “A” in panel D). The view covers ~60 km along the south rift flank and results from projecting 300 swath profiles perpendicularly to their strike, which is orthogonal to the main fault system (N105°E). Swath profiles are exaggerated ~8 times in the vertical. Areas of large topographic coherency along the footwall lead to whiter sectors. Thicker semi-transparent red lines highlight gently south-dipping sectors of coherent-in-depth topography that are consistent with the lower topographic heights along the footwall (flexed topography), and with the best-fit quadratic curves derived from the paleoshorelines in Fig. 3, in different colours (flexed paleoshorelines). The end of these sectors that is closer to the fault coincides with a topography change to steep slopes to the north. This topographic inflection is capped by the perched Gilbert-type deltas of Mavro and Evrostini. (B) View of topography perpendicular to the bounding fault strike for the eastern half of the main sector (shown in vertical stripes in D), constructed as described in A. This view uses 100 topographic swaths with a vertical exaggeration of ~5.5. (C) View of topography perpendicular to the bounding fault strike for the western half of the main sector (area of horizontal stripes in D), constructed as described in A. This view uses 100 topographic swaths with a vertical exaggeration of ~5.5. (D) Index map, with an indication of footwall area covered by each of the three stacked swaths.

## 5.2 Across-footwall river profiles

We analyze the geometry of the across-footwall river catchments (Fig. 5) using longitudinal profiles of rivers that drain the footwall orthogonally towards the active fault. The profile morphology and geometry of fault-orthogonal footwall river catchments depart from theoretical equilibrium, i.e. smooth-graded concave-upward profiles (Fig. 5A). All river profiles exhibit a principal inflection, defined as either a convex-up knickpoint zone or a windgap, marking a stark morphologic transition at ~15-25 km from the active fault (Fig. 5A). This principal inflection separates either (i) steep lower reaches from broad, low gradient upland reaches that have different degrees of back-tilt along the extensional footwall, or (ii) steep gulf-draining rivers from endorheic basins that record drainage inversion (Figs. 2 & 5). Overall, the principal inflection is located closer to the fault in the rift center, and farther away from it along strike (see white-grey contact for main river catchments in eastern and western main sector in Fig. 5A). Similarly, the degree of back tilt in low gradient reaches decreases along rift strike away from the short steep gulf-draining rivers and reversed drainages that dominate the rift center (Figs. 2, 5B, 5C). Given that most rivers steepen in response to enhanced rates of rock uplift (Snyder et al., 2000) and that the principal inflection mirrors the topography seemingly, we infer that the large knickpoints and windgaps are of common origin and result from a rapid increase in uplift rate along the full length of the master fault system.

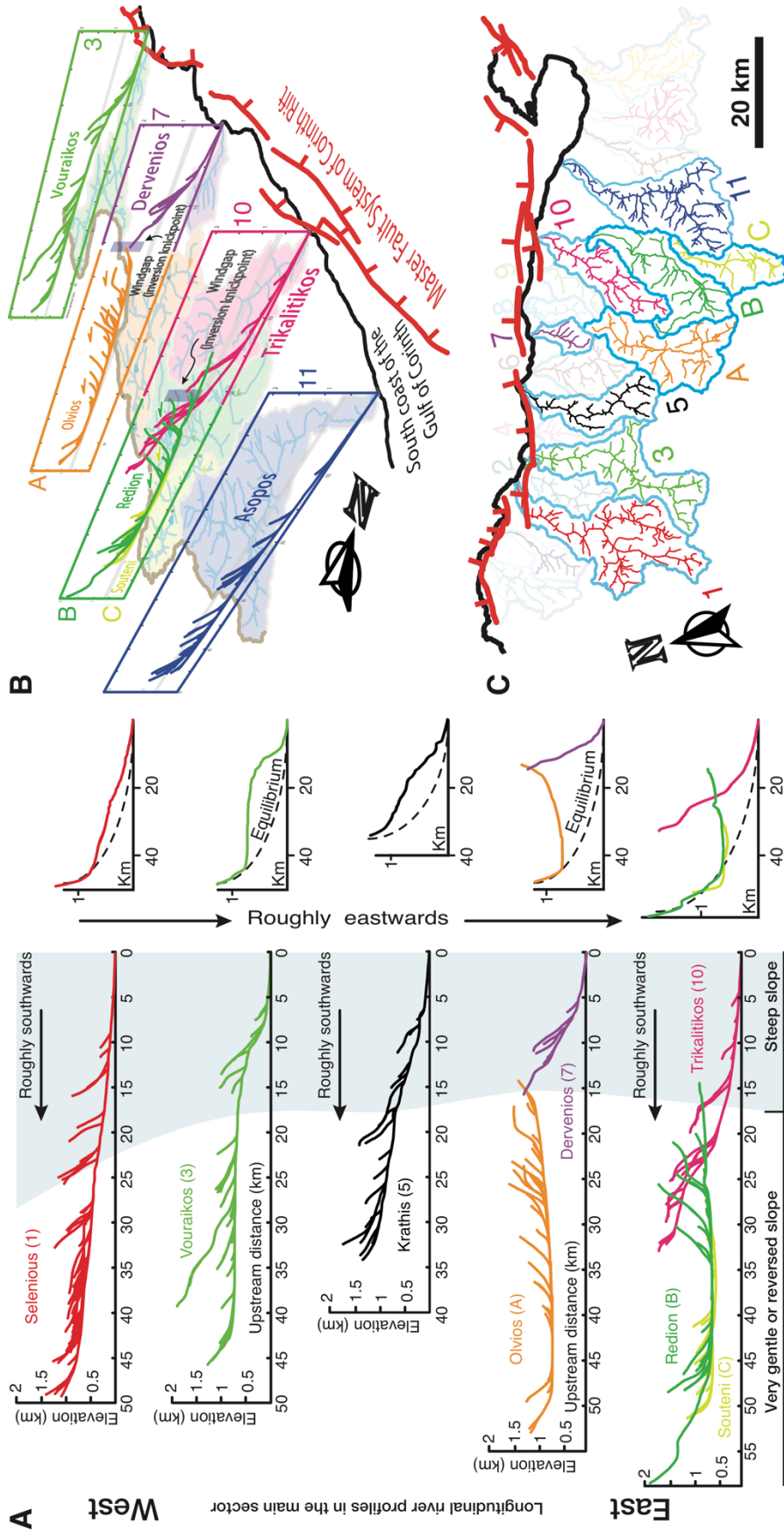


**Fig. 5. Across-footwall river profiles topography.** (A) River longitudinal profiles along the rift margin. River long profiles of 5 out of the 6 largest drainages in the rift margin, at the same scale and with their outlets aligned vertically, from the west (at the top) to the east (at the bottom). In the rift center, we plot reversed and beheaded rivers together. Plots to the right show the main trunks of the same rivers and the outline of their theoretical smooth-graded profiles of equilibrium. (B) 3D view of longitudinal profiles of river catchments and the plain view of their drainage areas, with regard to the master fault system. The view covers ~60 km along, and 50 km across, the main fault system. Note the prominent size of the reversed catchments in the center of the rift, both in upstream drainage longitudinal profiles and plain views. (C) Index map, with an indication of footwall river drainages used in A and B. Gulf-draining rivers are indicated with numbers; 1 - Selenious, 3 - Vouraikos, 5 - Krathis, 7 - Dervenios, 10 - Trikalitikos, 11 - Asopos. Reversed-flow river basins, now endorheic, are indicated with letters; A - Olvios, B - Redion, C - Souteni.

### 5.3 Along-footwall relief

We explore the geometry of the footwall along its strike using fault footwall relief (Fig. 6), approximated by the local elevation change from active fault to first major break-of-slope in the footwall topography. The along-footwall gradient in footwall relief (Fig. 6) varies in a systematic manner along the main rift sector and is consistent with a parabola. The along-footwall gradient of fault footwall relief, measured from the fault, shows an asymmetric parabola of wavelength >60 km. The parabola decays from the rift center, which is located at ~35 km from the west end of the main rift sector (Fig. 6). The footwall relief decays parabolically from its maximum height of ~2.5 km in the rift center to ~1.25 km and ~0.75 km in the east and west end of the main rift sector, respectively. Therefore, the current topography, when observed at the rift margin scale, is consistent with a pattern of fault slip that defines a cumulative parabolic displacement along the rift margin. This pattern is expected for long-term activity ( $\sim 10^6$  yr) along a single, high-angle fault system at margin scale.

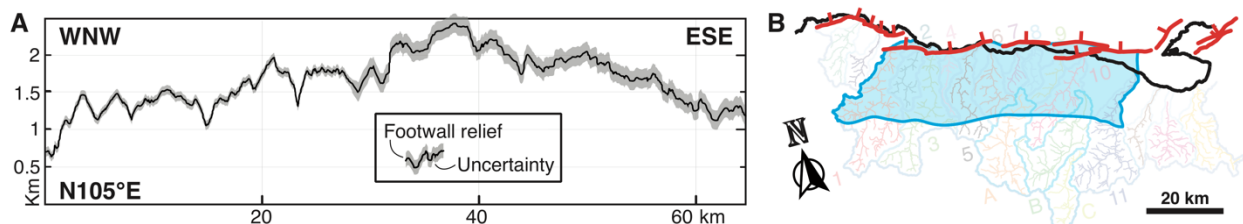


**Fig. 6. Footwall relief projected along the fault strike.** (A) Distribution of footwall relief along master fault strike. Footwall relief is the height difference between the principal inflection and the master fault trace, measured vertically. Uncertainty is estimated from fault mapping precision and the relative departure between fault strike and projection strike. See details in section 4.3. (B) Index map, with an indication of footwall area used for the calculus of footwall relief.

## 5.4 Along-footwall river profiles

We explore the geometry of the footwall along its strike projecting river networks and reversed basins towards the fault (Fig. 7). River profiles projected towards the fault show geometries that also respond to a parabolic pattern along the same footwall sector (Fig. 7). The upland reaches of the largest drainages have low gradient streams that occupy significant along-footwall distances (see rivers 1, 3 & 11 in Fig. 7), a morphology that resembles that of the reversed river drainages (A, B & C in Fig. 7). The elevation of these flat regions mark a morphological transition in drainage flow patterns, also for rivers where such flat regions are not evident (see rivers 2, 4, 5, 6, 8, 9 & 10 in Fig. 7). This cognac-glass valley morphology contrast with the wine-glass valleys observed in shorter rivers, and in the lower reaches of some of the longer drainages (see 2, 3, 4, 5 & 7 in Fig. 7). The elevation of the flat regions at the bottom of the cup of cognac-glass valleys vary consistently and in agreement with a parabola much like that defined by the footwall relief (cf. Fig. 6 & upper right inset in Fig. 7). Again, this parabolic pattern defines the cumulative fault slip, and thus fault uplift, expected for sustained activity ( $\sim 10^6$  yr) along a composite, kinematically-coherent, high-angle fault at rift scale.

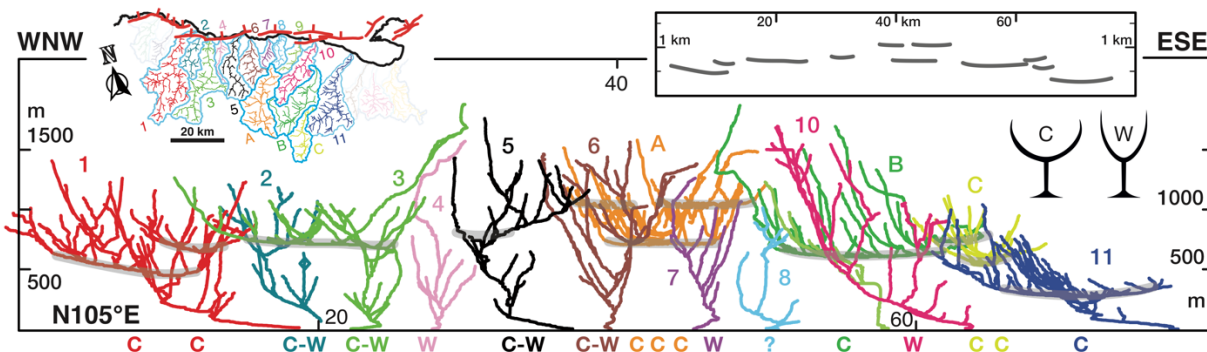


**Fig. 7. River profiles projected along the fault strike.** (A) Distribution of river longitudinal profiles along master fault strike. River longitudinal profiles projected along the fault strike in the main sector (N105°E), with 8 times vertical exaggeration. The morphology of the river valleys is indicated below the profile with the letters; (C) cognac-glass valleys; (W) wine-glass valleys; (C-W) cognac-glass valleys in upland reaches and wine-glass valleys in the lower reaches. River reaches that drain low-relief areas at the bottom of the cup of cognac-glass valleys are highlighted with thick semitransparent grey lines. Numbers and letters corresponds to those indicated in the index map in the upper left inset. This inset shows gulf-flowing rivers with numbers and reversed-flow drainages with letters as; 1 - Selenious, 2 - Kerinitis, 3 - Vouraikos, 4 - Ladopotamos, 5 - Krathis, 6 - Krios, 7 - Dervenios, 8 - Skoupeiko, 9 - Fonissa, 10 - Trikalitikos, and 11 - Asopos, A - Olvios, B - Redion, C - Souteni. The upper right inset shows the elevation of areas with low relief streams.

## 5.5 Along-footwall main inflection heights and kns below them

The elevation of the principal inflection is highest in the center of the modern rift and decays asymmetrically but systematically along the rift margin (Fig. 8A). The principal inflections have heights that correlate with the along-footwall parabolic pattern shown by the footwall relief, albeit at lower elevations. The pattern of lateral gradients in ksn of the downstream reaches is less clean (Fig. 8B), and we consider two possibilities. Either ksn of the downstream reaches portrays a parabolic decay from its center and River 3 (Vouraikos) is an outlier, or it shows a roughly linear increase towards River 3, and then abruptly decays. We consider the former more plausible than the latter, given the parabolic geometry of fault slip derived from other proxies. If our inference is correct, then the distribution of footwall metrics sensitive to relative uplift rates records along-footwall variations in flexural uplift that appear consistent with slip along a single, composite fault system acting at rift-margin scale. If not, only the knickpoint elevation shows the signal of slip along a rift-scale fault, and the kns values show a different signal, perhaps related to the known gradient in modern GPS velocities with an increase of  $0.5 \text{ mm}\times\text{yr}^{-1}$  westward (e.g., Avallone et al., 2004).

A finer along-footwall characterisation of flexure is precluded by effects due to river location relative to bounding fault trace, recent drainage reversals, changes in drainage area and/or local faulting. For example, the Vouraikos and Fonissa ksn values (3 and 9 in Fig. 8B) are two outliers that we interpret as the result of a recent increase in uplift rate magnitude by fault linkage and a recent increase in drainage area, respectively. However, whereas the latter interpretation seems plausible, the former is only tentative, as the river crosses a continuous trace in the East Helike Fault. Another significant effect is the drainage reorganization and large river reversals that have occurred in some rivers east of River 6 (Fig. 2). We expect larger ksn values for equilibrated river catchments that recently lost drainage area in this region (beheaded rivers 6 to 10, Fig. 8C). Larger uncertainties exist for the same area east of River 6, as the fault increases in distance from river outlets. Finally, local effects may affect the Asopos River (11 in Fig. 8A, C) since it lays at the tip of the fault sector

considered, and where the fault is underwater and away from the river outlet. Either or both these facts may lead to the low elevations of the river main inflection, precluding a clean interpretation. Therefore, while the along-footwall parabolic distributions (Figs. 6, 7 & 8A) are consistent with maximum cumulative footwall flexural uplift and uplift rate in the rift center, we attribute larger confidence to the finite geometry of the western half of the parabola.

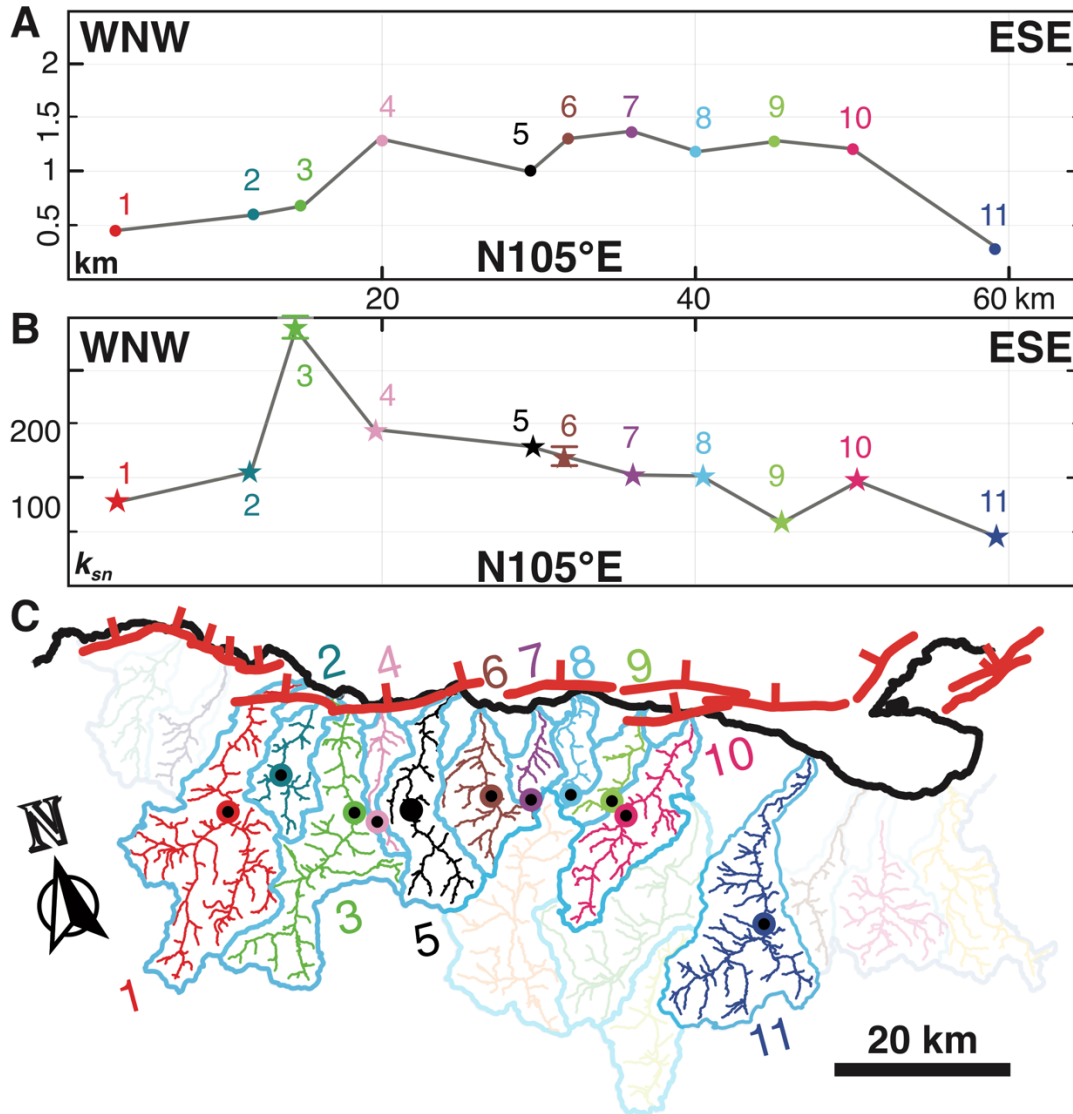


**Fig. 8. Height of, and  $k_{sn}$  of streams below, main inflections projected along the fault strike.** (A) Height of the main inflection and (B) normalized steepness index ( $k_{sn}$ ) of river reaches below each inflection, both projected at the river outlets orthogonally to the main fault system (N105°E). Error bars are smaller than the symbols in both plots in all cases except for rivers 3 and 6 in panel B. (C) Index map, with an indication of footwall river drainages used in A and B, and location of the main inflection in map view. Numbers show the gulf-draining rivers of 1 - Selenious, 2 - Kerinitis, 3 - Vouraikos, 4 - Ladopotamos, 5 - Krathis, 6 - Krios, 7 - Dervenios, 8 - Skoupeiko, 9 - Fonissa, 10 - Trikalitikos, and 11 - Asopos. The main inflection is indicated with circles.



## 6 Discussion

Our geomorphologic evidence novelly outlines the flexural uplift geometry by early intracontinental rifting in the Corinth Rift: a continental lithosphere that coherently up-bends across the rift (>50 km) and has a parabolic decay along the rift (>60 km) throughout faulting ( $\sim 10^6$  yr). Such flexure pattern at rift margin scale sets the geometry of its topography and river profiles, and the magnitude of geomorphic proxies for uplift, uplift rate and fault displacement.

### 6.1 Implications for the Corinth Rift

The landscape of the Corinth Rift southern margin evolves in response to flexure (Figs. 1A & 9). Footwall topography and river drainages show morphologies (Figs. 4 to 8) that are consistent with a cumulative signal of flexural uplift that is spatially coherent over most of the rift; an exponential increase towards the fault and a parabolic decay from the rift centre along its strike (Fig. 9). The across-footwall flexure signal is unequivocal in the topography for >60 km along footwall (Fig. 4), and caused river profiles to adjust by steepening their lower reaches and forcing a marked back-tilt in their upper reaches that decays along strike (Fig. 5). Conspicuous drainage reversals landward of gulf-flowing beheaded drainages occur in the rift center, where the topographic expression of flexure is most prominent (Figs. 4 & 5). Both the location of drainage reversals and the different degrees of landward tilting in the upstream reaches correlate positively with the height of footwall relief and the main inflections of river profile measured from the fault (Figs. 5 to 8A). Collectively, the above suggest that maximum slip rates occur at the rift center and led to flexural uplift rates that are also the largest in the rift center (Fig. 9). This agrees well with previous research that suggested larger uplift in the rift center (R. Armijo et al., 1996; e.g., Dufaure, 1975; Pirazzoli et al., 2004). We infer that large flexural uplift rates exceeding river incision capabilities result in drainage reversal of inland reaches (Fig. 9). This is supported by numerical models (Cowie et al., 2006).

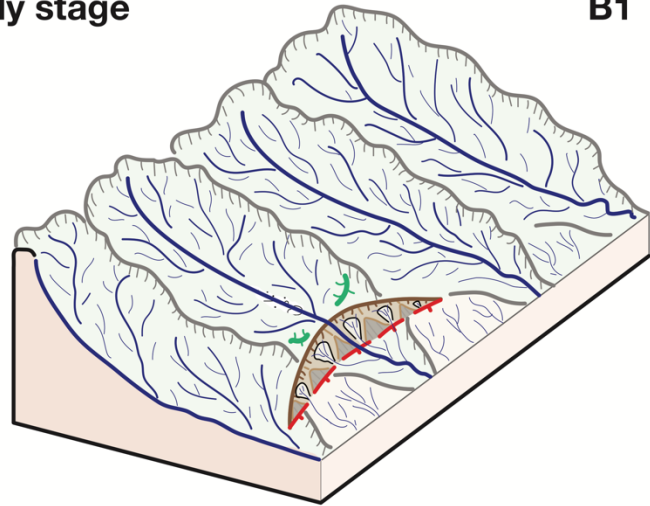
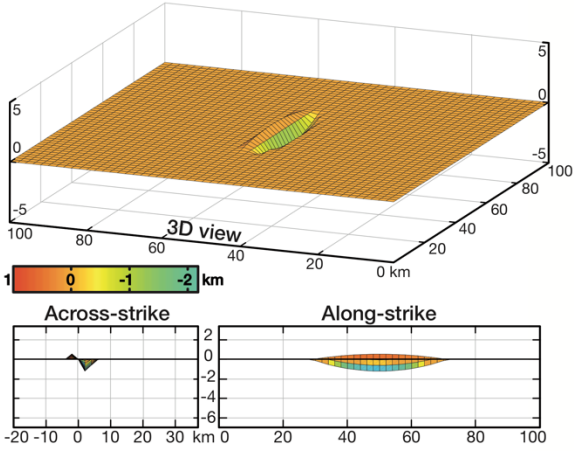
### 3D FLEXURE GEOMETRY

### FLUVIAL LANDSCAPE EVOLUTION

A1

Early stage

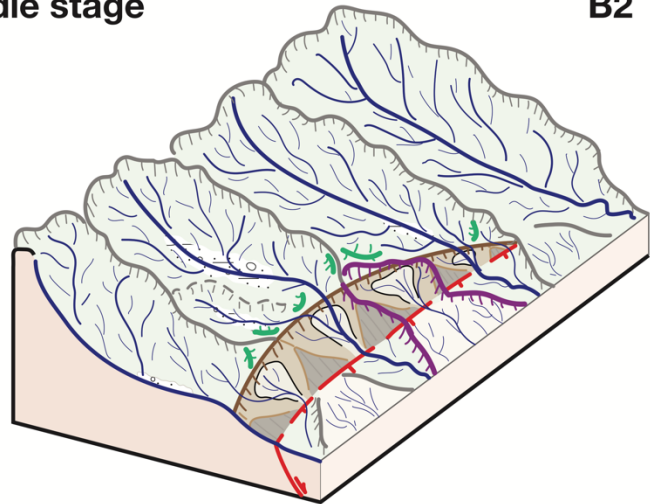
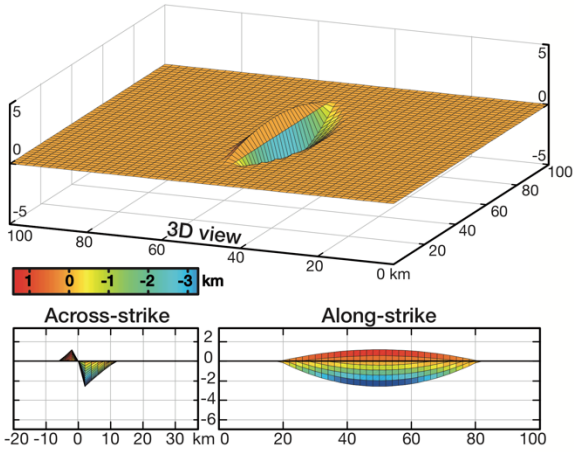
B1



A2

Middle stage

B2



A3

Late stage

B3

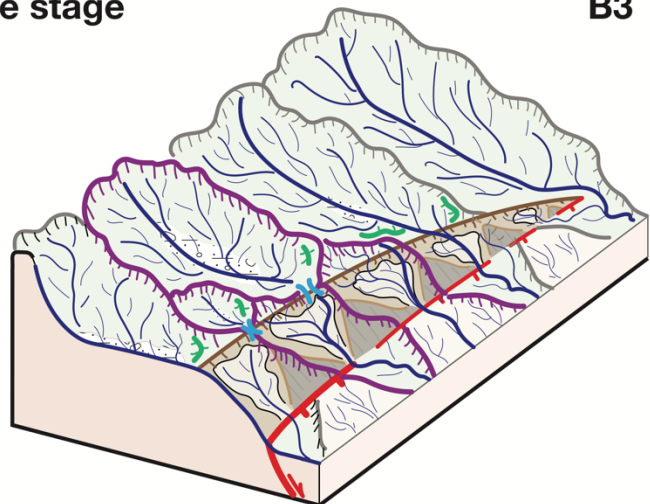
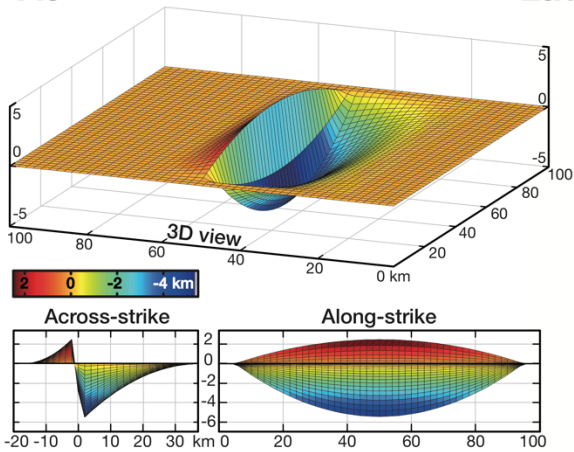


**Fig. 9. 3D geometry of flexural uplift by continental rifting and its effect on landscapes.** Evolutionary block diagrams that schematically show; (A) the 3D geometry of flexure in relation to extensional faulting in continents, and (B) its effects on a sector of a fluvial landscape. (A) Block models showing the geometry of flexure in 3D, and its associated across- and along-footwall views. Each block diagram has an horizontal grid 100 km wide in both directions with squares of 2 x 2 km, and extends 10 km in the vertical direction, that is exaggerated 3 times. The 3D flexural geometry couples the across-footwall exponential flexure defined by De Gelder et al. (2019) and a quadratic curve that fits the along-footwall parabolic geometry of the fault footwall derived here (see Fig. 6). We obtain the hanging-wall flexure geometry using the same geometric constraints and an assumed uplift-to-subsidence ratio of 1:2.2, i.e. the average between calculated values for the rift; 1:1.2-2.4 (De Gelder et al., 2019) and 1:2-3.2 (McNeill & Collier, 2004). The fault locates at the center of the grid and has a maximum surficial length of (A1) 30 km, (A2) 60 km, and (A3) 90 km, but the fault trace and fault plane are not shown. Along-strike panels show a composite view of the appearance of the footwall (for the panel sector above 0 m) and the hanging-wall (for the panel sector below 0 m) that look orthogonally towards the fault in both cases. The initial and intermediate growth stages (A1 & A2) are scaled versions of A3 and their flexural geometry is unconstrained. (B) Block models of a fluvial landscape evolving in relation to the growth of the crustal normal fault and its associated lithospheric flexure in (A). The hanging wall flexural subsidence and the location of sea level are not represented, for simplicity, and the frontal view locates on a river trunk. The fault is in red and the footwall relief is shown in brown colors, with darker tones for the triangular facets and lighter tones for small river drainages formed on the fault relief. Rivers are in blue and their drainage divides in light grey for inherited drainages and in purple for fault-formed drainages. Thick green lines represent areas with streams that drain in reverse direction and windgaps are shown with thick blue lines.

The flexural model apposite at rift scale (Fig. 9) yields novel inferences on rift mechanics. The distributions of flexural uplift and slip rates are consistent with well-known relationships for single fault systems (Figs. 3 to 8) (e.g., Cowie & Scholz, 1992; Dawers et al., 1993; Densmore et al., 2004; Roberts & Michetti, 2004), thus defining a single, high-angle fault system kinematically-linked at rift scale (Figs. 1A & 8). This finding is hitherto unreported for the Corinth Rift. Inherited relief resulting from distributed faulting (e.g., Gawthorpe et al., 1994; Goldsworthy & Jackson, 2001) in relation to Aegean Sea back-arc extension (e.g. Brun & Sokoutis, 2010; Jolivet et al., 2013) is limited and in stark contrasts with the modern short-wavelength, high-amplitude rift relief (Fig. 4). This was observed by early works in the area (e.g., Ori, 1989), and together with the morphological similarity between footwall topography and river profiles (cf. Figs. 4 & 5) supports a young and fast growth of the modern rift margin. These observations, in turn, suggest a subsidiary role for regional uplift (e.g., Turner et al., 2010) and paleo-relief (e.g., Ghisetti & Vezzani, 2005) in the modern rift evolution (Fig. 9).

The remarkable consistency of the cumulative elastic flexure signal observed in the across-footwall topography along the rift margin and its coherency with its shorter-term signal set by Pleistocene marine terraces (Fig. 4) implies highly-localized strain in the master fault system since

its onset (Fig. 9). This agrees with previous studies on rift bounding-fault localization (e.g., Roberts et al., 2009). Moreover, modelling studies show that long-term, large-scale flexural footwall uplift, as the one reported here for the rift margin in Corinth (Fig. 9), requires repeated coseismic slip on localized high-angle faults that reach at least the brittle-ductile transition (Bell et al., 2017; De Gelder et al., 2019; King et al., 1988), and an isostatic elastic response of the whole crust (e.g., King & Ellis, 1990). Collectively, the above implies the master fault transects the crust to the brittle-ductile transition in a lithosphere with consistent large strength in space, at rift scale (>50 km), and time, throughout faulting ( $\sim 10^6$  yr).

## 6.2 Implications for early continental rifting

Geometric characterisations of flexure similar to that presented here (Fig. 9) hold the potential to deepen our understanding on the relationships between landscape evolution, elastic flexure and faulting in actively extending regions, such as the Basin and Range, the East African and Baikal rifts or Tibet. For example, the prime information on rheology, mechanics or dynamics derived from the geometry of topography in areas of up-flexed continental lithosphere (Armijo et al., 1996; Brown & Phillips, 1999; De Gelder et al., 2019; Masek et al., 1994; Owens, 1983; ter Voorde et al., 1998; Zandt & Owens, 1980) is limited by the time span and spatial extent (2D transects) of the markers used. Contrarily, our approach provides constraints on the along-footwall geometry, extent and coherency of the flexural uplift signal (Figs. 4 to 9), that in turn relate with rift-scale long-term lithospheric strength, length and down-dip geometry of the accommodating fault(s), and crustal-scale strain localisation, respectively.

Our work illustrates that the evolving elastic flexure associated with regional-scale faults (tens of km) during long-term ( $10^4$ - $10^6$  yr) extension of continental lithosphere is recorded in their uplifting landscapes. Corinth landscape unparalleled record of flexural uplift and highly-localized strain suggest that these processes are intrinsic to the earliest stages of continental rifting. These

processes may be masked in other sites or at later stages by ambiguous geomorphological evidence and/or denudation. Prominent reversals of river catchments in older and low-extending rifts and individual grabens, as the East African Rift and South Tibet (Armijo et al., 1986; Doornkamp & Temple, 1966), can be explained if elastic flexure and localized strain occurred at their early stages of intracontinental rifting. The generalization of elastic flexure processes to intracontinental extension areas of any age or extension rate implies that the process of rifting is highly localized in strain, and disruptive in space and possibly in time.

## 7 Conclusion

We provide a finer characterisation of flexure geometry by intracontinental rifting and its associated flexural uplift signal during fault activity ( $10^4$ - $10^6$  yr) and virtually in three-dimensions (tens of km). We explore the geomorphic expression of flexure throughout the landscape of the southern margin of the Corinth Rift, and using new and conventional representations of standard approaches aimed at highlighting the simple geometrical relationships between geomorphic elements in extensional footwalls and their active normal faults. We use the observed geometric relationships to novelly define the evolving, combined effect of progressive flexure and uplift at the scale of the rift margin, thereby characterizing the geometry of flexure at rift scale. The signal of flexure is very coherent in space and time, implying highly-localized strain in a crustal-scale, high-angle normal fault affecting continental lithosphere with long-term strength to the base of the seismogenic layer or deeper. Considering this record of flexure unique worldwide, we generalise flexural uplift and strain localisation as intrinsic processes of early intracontinental rifting in nature.

## Acknowledgements

We thank Patience Cowie for discussions and the detailed comments of three anonymous reviewers on an earlier version of the manuscript. The research leading to these study has received funding from the People Programme (Marie Curie Actions) of the European Union's Seventh Framework Programme under the ITN project ALerT (Grant FP7-PEOPLE-2013-ITN number 607996) and by the ISIS program of the CNES. This study contributes to the IdEx Université de Paris ANR-18-IDEX-0001.

This is IPGP contribution \*\*\*\*\*

## References

- Armijo, R., Lacassin, R., Coudurier-Curveur, A., & Carrizo, D. (2015). Coupled tectonic evolution of Andean orogeny and global climate. *Earth-Science Reviews*, *143*, 1–35.
- Armijo, R., Tapponnier, P., Mercier, J. L., & Han, T.-L. (1986). Quaternary extension in southern Tibet: Field observations and tectonic implications. *Journal of Geophysical Research*, *91*(B14), 13803–13872.
- Armijo, R., Lyon-Caen, H., & Papanastassiou, D. (1991). A possible normal-fault rupture for the 464 BC Sparta earthquake. *Nature*, *351*(6322), 137–139.
- Armijo, R., Meyer, B., King, G. C. P., Rigo, A., & Papanastassiou, D. (1996). Quaternary evolution of the Corinth Rift and its implications for the Late Cenozoic evolution of the Aegean. *Geophysical Journal International*, *126*(1), 11–53.
- Attal, M., Tucker, G. E., Whittaker, A. C., Cowie, P. A., & Roberts, G. P. (2008). Modeling fluvial incision and transient landscape evolution: Influence of dynamic channel adjustment. *Journal of Geophysical Research*, *113*(F3), F02010.
- Avallone, A., Briole, P., Agatza-Balodimou, A. M., Billiris, H., Charade, O., Mitsakaki, C., et al. (2004). Analysis of eleven years of deformation measured by GPS in the Corinth Rift Laboratory area. *Comptes Rendus: Geoscience*, *336*(4–5), 301–311.
- Bell, R. E., Duclaux, G., Nixon, C. W., Gawthorpe, R. L., & McNeill, L. C. (2017). High-angle, not low-angle, normal faults dominate early rift extension in the Corinth Rift, central Greece. *Geology*. <https://doi.org/10.1130/G39560.1>
- Bernard, P., Lyon-Caen, H., Briole, P., Deschamps, A., Boudin, F., Makropoulos, K., et al. (2006). Seismicity, deformation and seismic hazard in the western rift of Corinth: New insights from the Corinth Rift Laboratory (CRL). *Tectonophysics*, *426*(1–2), 7–30.
- Boulton, S. J., & Whittaker, A. C. (2009). Quantifying the slip rates, spatial distribution and evolution of active normal faults

- from geomorphic analysis: Field examples from an oblique-extensional graben, southern Turkey. *Geomorphology*, 104(3–4), 299–316.
- Brown, C. D., & Phillips, R. J. (1999). Flexural rift flank uplift at the Rio Grande rift, New Mexico. *Tectonics*, 18(6), 1275–1291.
- Brun, J.-P., & Sokoutis, D. (2010). 45 m.y. of Aegean crust and mantle flow driven by trench retreat. *Geology*, 38(9), 815–818.
- Buck, W. R. (1993). Effect of lithospheric thickness on the formation of high- and low-angle normal faults. *Geology*, 21(10), 933–936.
- Bürgmann, R., Pollard, D. D., & Martel, S. J. (1994). Slip distributions on faults: effects of stress gradients, inelastic deformation, heterogeneous host-rock stiffness, and fault interaction. *Journal of Structural Geology*, 16(12), 1675–1690.
- Charalampakis, M., Lykousis, V., Sakellariou, D., Papatheodorou, G., & Ferentinos, G. (2014). The tectono-sedimentary evolution of the Lechaion Gulf, the south eastern branch of the Corinth graben, Greece. *Marine Geology*, 351, 58–75.
- Cowie, P. A., & Scholz, C. H. (1992). Displacement-length scaling relationship for faults: data synthesis and discussion. *Journal of Structural Geology*, 14(10), 1149–1156.
- Cowie, P. A., Attal, M., Tucker, G. E., Whittaker, A. C., Naylor, M., Ganas, A., & Roberts, G. P. (2006). Investigating the surface process response to fault interaction and linkage using a numerical modelling approach. *Basin Research*, 18(3), 231–266.
- Crosby, B. T., & Whipple, K. X. (2006). Knickpoint initiation and distribution within fluvial networks: 236 waterfalls in the Waipaoa River, North Island, New Zealand. *Geomorphology*, 82(1), 16–38.
- Dawers, N. H., & Anders, M. H. (1995). Displacement-length scaling and fault linkage. *Journal of Structural Geology*, 17(5), 607–614.
- Dawers, N. H., Anders, M. H., & Scholz, C. H. (1993). Growth of normal faults: Displacement-length scaling. *Geology*, 21(12), 1107–1110.
- De Gelder, G., Fernández-Blanco, D., Melnick, D., Duclaux, G., Bell, R., Jara-Muñoz, J., et al. (2019). Lithospheric flexure and rheology determined by climate cycle markers in the Corinth Rift. *Scientific Reports*, --(--), -.
- Demoulin, A., Beckers, A., & Hubert-Ferrari, A. (2015). Patterns of Quaternary uplift of the Corinth rift southern border (N Peloponnese, Greece) revealed by fluvial landscape morphometry. *Geomorphology*, 246, 188–204.
- Densmore, A. L., Dawers, N. H., Gupta, S., Guidon, R., & Goldin, T. (2004). Footwall topographic development during continental extension. *Journal of Geophysical Research*, 109(F3), F03001.
- Densmore, A. L., Dawers, N. H., Gupta, S., & Guidon, R. (2005). What sets topographic relief in extensional footwalls?

- Geology*, 33(6), 453–456.
- DiBiase, R. A., Whipple, K. X., Heimsath, A. M., & Ouimet, W. B. (2010). Landscape form and millennial erosion rates in the San Gabriel Mountains, CA. *Earth and Planetary Science Letters*, 289(1), 134–144.
- Doornkamp, J. C., & Temple, P. H. (1966). Surface, Drainage and Tectonic Instability in Part of Southern Uganda. *The Geographical Journal*, 132(2), 238–252.
- Doutsos, T., & Piper, D. J. W. (1990). Listric faulting, sedimentation, and morphological evolution of the Quaternary eastern Corinth rift, Greece: First stages of continental rifting. *Geological Society of America Bulletin*, 102(6), 812–829.
- Dufaure, J.-J. (1975). *Le relief du Péloponèse* (Thèse Lettres). Université Paris IV.
- Dufaure, J.-J. (1977). Néotectonique et morphogenèse dans une péninsule méditerranéenne: Le Péloponnèse. *Revue de Géographie Physique et de Géologie Dynamique*, 19, 27–58.
- Flint, J. J. (1974). Stream gradient as a function of order, magnitude, and discharge. *Water Resources Research*, 10(5), 969–973.
- Ford, M., Rohais, S., Williams, E. A., Bourlange, S., Jouselin, D., Backert, N., & Malartre, F. (2012). Tectono-sedimentary evolution of the western Corinth rift (Central Greece). *Basin Research*, 0, 1–23.
- Ford, M., Hemelsdaël, R., Mancini, M., & Palyvos, N. (2016). Rift migration and lateral propagation: evolution of normal faults and sediment-routing systems of the western Corinth rift (Greece). *Geological Society, London, Special Publications*, 439. <https://doi.org/10.1144/SP439.15>
- Forsyth, D. W. (1992). Finite extension and low-angle normal faulting. *Geology*, 20(1), 27–30.
- Gallen, S. F., & Wegmann, K. W. (2017). River profile response to normal fault growth and linkage: An example from the Hellenic forearc of south-central Crete, Greece. *Earth Surface Dynamics*, 5(1), 161.
- Gawthorpe, R., Fraser, A., & Collier, R. (1994). Sequence stratigraphy in active extensional basins: implications for the interpretation of ancient basin-fills. *Marine and Petroleum Geology*, 11(6), 642–658.
- Gawthorpe, R. L., Leeder, M., Kranis, H., Skourtsos, E., Andrews, J., Henstra, G., et al. (2017). Tectono-sedimentary evolution of the Plio-Pleistocene Corinth rift, Greece. *Basin Research*. <https://doi.org/10.1111/bre.12260>
- Ghisetti, F., & Vezzani, L. (2005). Inherited structural controls on normal fault architecture in the Gulf of Corinth (Greece). *Tectonics*, 24(4), TC4016.
- Goldsworthy, M., & Jackson, J. (2001). Migration of activity within normal fault systems: examples from the Quaternary of mainland Greece. *Journal of Structural Geology*, 23, 489–506.
- Goren, L., Fox, M., & Willett, S. D. (2014). Tectonics from fluvial topography using formal linear inversion: Theory and applications to the Inyo Mountains, California. *Journal of Geophysical Research: Earth Surface*, 119(8), 1651–1681.
- Gupta, A., & Scholz, C. H. (2000). A model of normal fault interaction based on observations and theory. *Journal of*



*Structural Geology*, 22(7), 865–879.

- Hemelsdaël, R., Ford, M., Malartre, F., & Gawthorpe, R. (2017). Interaction of an antecedent fluvial system with early normal fault growth: Implications for syn-rift stratigraphy, western Corinth rift (Greece). *Sedimentology*, 64(7), 1957–1997.
- Howard, A. D. (1994). A detachment-limited model of drainage basin evolution. *Water Resources Research*, 30(7), 2261–2285.
- Jolivet, L., & Brun, J.-P. (2010). Cenozoic geodynamic evolution of the Aegean. *International Journal of Earth Sciences*, 99(1), 109–138.
- Jolivet, L., Faccenna, C., Huet, B., Labrousse, L., Le Pourhiet, L., Lacombe, O., et al. (2013). Aegean tectonics: Strain localisation, slab tearing and trench retreat. *Tectonophysics*, 597–598, 1–33.
- Kent, E., Boulton, S. J., Whittaker, A. C., Stewart, I. S., & Cihat Alçiçek, M. (2016). Normal fault growth and linkage in the Gediz (Alaşehir) Graben, Western Turkey, revealed by transient river long-profiles and slope-break knickpoints. *Earth Surface Processes and Landforms*. <https://doi.org/10.1002/esp.4049>
- King, G., & Ellis, M. (1990). The origin of large local uplift in extensional regions. *Nature*, 348(6303), 689–693.
- King, G. C. P., Stein, R. S., & Rundle, J. B. (1988). The Growth of Geological Structures by Repeated Earthquakes 1. Conceptual Framework. *Journal of Geophysical Research*, 93(B11), 13307–13318.
- Kirby, E., & Whipple, K. X. (2001). Quantifying differential rock-uplift rates via stream profile analysis. *Geology*, 29(5), 415–418.
- Kirby, E., & Whipple, K. X. (2012). Expression of active tectonics in erosional landscapes. *Journal of Structural Geology*, 44, 54–75.
- Le Pichon, X., & Angelier, J. (1981). The Aegean Sea. *Philosophical Transactions of the Royal Society of London A: Mathematical, Physical and Engineering Sciences*, 300(1454), 357–372.
- Manighetti, I., King, G. C. P., Gaudemer, Y., Scholz, C. H., & Doubre, C. (2001). Slip accumulation and lateral propagation of active normal faults in Afar. *Journal of Geophysical Research*, 106(B7), 13667–13696.
- Masek, J. G., Isacks, B. L., Fielding, E. J., & Browaeys, J. (1994). Rift flank uplift in Tibet: Evidence for a viscous lower crust. *Tectonics*, 13(3), 659–667.
- McNeill, L. C., & Collier, R. E. L. (2004). Uplift and slip rates of the eastern Eliki fault segment, Gulf of Corinth, Greece, inferred from Holocene and Pleistocene terraces. *Journal of the Geological Society*, 161(1), 81–92.
- Miller, S. R., Baldwin, S. L., & Fitzgerald, P. G. (2012). Transient fluvial incision and active surface uplift in the Woodlark Rift of eastern Papua New Guinea. *Lithosphere*. <https://doi.org/10.1130/1135.1>
- Niemann, J. D., Gasparini, N. M., Tucker, G. E., & Bras, R. L. (2001). A quantitative evaluation of Playfair's law and its use in

- testing long-term stream erosion models. *Earth Surface Processes and Landforms: The Journal of the British Geomorphological Research Group*, 26(12), 1317–1332.
- Nixon, C. W., McNeill, L. C., Bull, J. M., Bell, R. E., Gawthorpe, R. L., Henstock, T. J., et al. (2016). Rapid spatiotemporal variations in rift structure during development of the Corinth Rift, central Greece. *Tectonics*, 35(5).  
<https://doi.org/10.1002/2015TC004026>
- Ori, G. G. (1989). Geologic history of the extensional basin of the Gulf of Corinth (?Miocene-Pleistocene), Greece. *Geology*, 17(10), 918–921.
- Ouimet, W. B., Whipple, K. X., & Granger, D. E. (2009). Beyond threshold hillslopes: Channel adjustment to base-level fall in tectonically active mountain ranges. *Geology*, 37(7), 579–582.
- Owens, T. J. (1983). Normal faulting and flexure in an elastic-perfectly plastic plate. *Tectonophysics*, 93(1), 129–150.
- Pechlivanidou, S., Cowie, P. A., Duclaux, G., Nixon, C. W., Gawthorpe, R. L., & Salles, T. (2019). Tipping the balance: Shifts in sediment production in an active rift setting. *Geology*, 47(3), 259–262.
- Perron, J. T., & Royden, L. (2013). An integral approach to bedrock river profile analysis. *Earth Surface Processes and Landforms*, 38(6), 570–576.
- Petit, C., & Ebinger, C. (2000). Flexure and mechanical behavior of cratonic lithosphere: Gravity models of the East African and Baikal rifts. *Journal of Geophysical Research*, 105(B8), 19151–19162.
- Pirazzoli, P. A., Stiros, S. C., Fontugne, M., & Arnold, M. (2004). Holocene and Quaternary uplift in the central part of the southern coast of the Corinth Gulf (Greece). *Marine Geology*, 212(1–4), 35–44.
- Roberts, G. P., & Michetti, A. M. (2004). Spatial and temporal variations in growth rates along active normal fault systems: an example from The Lazio–Abruzzo Apennines, central Italy. *Journal of Structural Geology*, 26(2), 339–376.
- Roberts, G. P., Houghton, S. L., Underwood, C., Papanikolaou, I., Cowie, P. A., van Calsteren, P., et al. (2009). Localization of Quaternary slip rates in an active rift in 105 years: An example from central Greece constrained by 234U-230Th coral dates from uplifted paleoshorelines. *Journal of Geophysical Research: Solid Earth*, 114(B10). Retrieved from <http://onlinelibrary.wiley.com/doi/10.1029/2008JB005818/full>
- Roda-Boluda, D. C., & Whittaker, A. C. (2017). Structural and geomorphological constraints on active normal faulting and landscape evolution in Calabria, Italy. *Journal of the Geological Society*, 174(4), 701–720.
- Rohais, S., Joannin, S., Colin, J.-P., Suc, J.-P., Guillocheau, F., & Eschard, R. (2007). Age and environmental evolution of the syn-rift fill of the southern coast of the gulf of Corinth (Akrata-Derveni region, Greece). *Bulletin de La Société Géologique de France*, 178(3), 231–243.
- Rosenbloom, N. A., & Anderson, R. S. (1994). Hillslope and channel evolution in a marine terraced landscape, Santa Cruz, California. *Journal of Geophysical Research*, 99(B7), 14013–14029.

- Schwanghart, W., & Scherler, D. (2014). TopoToolbox 2 – MATLAB-based software for topographic analysis and modeling in Earth surface sciences. *Earth Surface Dynamics*, 2(1), 1–7.
- Seger, M., & Alexander, J. (1993). Distribution of Plio-Pleistocene and Modern coarse-grained deltas south of the Gulf of Corinth, Greece. *Tectonic Controls and Signatures in Sedimentary Successions*, 20, 37–48.
- Snyder, N. P., Whipple, K. X., Tucker, G. E., & Merritts, D. J. (2000). Landscape response to tectonic forcing: Digital elevation model analysis of stream profiles in the Mendocino triple junction region, northern California. *GSA Bulletin*, 112(8), 1250–1263.
- Stein, R. S., King, G. C. P., & Rundle, J. B. (1988). The growth of geological structures by repeated earthquakes 2. Field examples of continental dip-slip faults. *Journal of Geophysical Research, [Solid Earth]*, 93(B11), 13319–13331.
- Stewart, J. H. (1978). 1: Basin-range structure in western North America: A review. *Geological Society of America Memoirs*, 152, 1–32.
- Taylor, B., Weiss, J. R., Goodliffe, A. M., Sachpazi, M., Laigle, M., & Hirn, A. (2011). The structures, stratigraphy and evolution of the Gulf of Corinth rift, Greece: Structures, stratigraphy and evolution of GoC. *Geophysical Journal International*, 185(3), 1189–1219.
- Tetreault, J. L., & Buitert, S. J. H. (2018). The influence of extension rate and crustal rheology on the evolution of passive margins from rifting to break-up. *Tectonophysics*, 746, 155–172.
- Thompson, G. A., & Parsons, T. (2016). Vertical deformation associated with normal fault systems evolved over coseismic, postseismic, and multiseismic periods. *Journal of Geophysical Research, Solid Earth*, 121(3), 2153–2173.
- Tucker, G. E., & Whipple, K. X. (2002). Topographic outcomes predicted by stream erosion models: Sensitivity analysis and intermodel comparison. *Journal of Geophysical Research*, 107(B9), 2179.
- Turner, J. A., Leeder, M. R., Andrews, J. E., Rowe, P. J., Van Calsteren, P., & Thomas, L. (2010). Testing rival tectonic uplift models for the Lechaion Gulf in the Gulf of Corinth rift. *Journal of the Geological Society*, 167(6), 1237–1250.
- ter Voorde, M., van Balen, R. T., Bertotti, G., & Cloetingh, S. A. P. L. (1998). The influence of a stratified rheology on the flexural response of the lithosphere to (un)loading by extensional faulting. *Geophysical Journal International*, 134(3), 721–735.
- Wallace, R. E. (1978). Geometry and rates of change of fault-generated range fronts, north-central Nevada. *J. Res. US Geol. Surv*, 6(5), 637–650.
- Weissel, J. K., & Karner, G. D. (1989). Flexural uplift of rift flanks due to mechanical unloading of the lithosphere during extension. *Journal of Geophysical Research*, 94(B10), 13919–13950.
- Whipple, K. X. (2004). Bedrock rivers and the geomorphology of active orogens. *Annual Review of Earth and Planetary Sciences*, 32(1), 151–185.

- Whipple, K. X., & Tucker, G. E. (1999). Dynamics of the stream-power river incision model: Implications for height limits of mountain ranges, landscape response timescales, and research needs. *Journal of Geophysical Research: Solid Earth*, *104*(B8), 17661–17674.
- Whittaker, A. C. (2012). How do landscapes record tectonics and climate? *Lithosphere*, *4*(2), 160–164.
- Whittaker, A. C., & Walker, A. S. (2015). Geomorphic constraints on fault throw rates and linkage times: Examples from the Northern Gulf of Evia, Greece. *Journal of Geophysical Research: Earth Surface*, *120*(1).  
<https://doi.org/10.1002/2014JF003318>
- Whittaker, A. C., Attal, M., Cowie, P. A., Tucker, G. E., & Roberts, G. (2008). Decoding temporal and spatial patterns of fault uplift using transient river long profiles. *Geomorphology*, *100*(3), 506–526.
- Wobus, C., Whipple, K. X., Kirby, E., Snyder, N., Johnson, J., Spyropolou, K., et al. (2006). Tectonics from topography: Procedures, promise, and pitfalls. *Geological Society of America Special Papers*, *398*, 55–74.
- Zandt, B. Y. G., & Owens, T. J. (1980). Crustal flexure associated with normal faulting and implications for seismicity along the Wasatch front, Utah. *Bulletin of the Seismological Society of America*, *70*(5), 1501–1520.